2 The use of synchrotron radiation for materials research

C. Riekel

2.1 Introduction

X-ray photons interact with matter in various ways (Figure 2.1). An analysis of these interactions allows the development of microscopic models, which serve to provide a better understanding of the physical properties of materials. In the following text, emphasis will be put on synchrotron radiation (SR) experiments with "hard" X-rays. "Hard" X-rays have, for the purpose of this text, wavelength of $\lambda \leq 0.25$ nm, which corresponds roughly to the spectral cut-off of a beryllium vacuum-window, which separates the SR source (see below) from the beamline optics. These wavelengths are, furthermore, on the same length scale as interatomic distances which allows high resolution structural studies.

The specific properties of SR can be summarized as:

- high brilliance;[1]
- pulsed radiation with pulse length down to about 0.1 ns range;
- extended spectral range;
- polarization.

These properties allow experiments which are complementary to experiments at laboratory X-ray sources.

2.2 Production of synchrotron radiation [1–3]

Synchrotron radiation is generated by bunches of electrons (or positrons) which circulate at relativistic energies close to the speed of light. In the simplest case, the electrons follow a circular orbit, which is defined by dipole magnets. As shown in Figure 2.2, the emitted radiation covers a range from the infrared to γ-rays. It is concentrated in a cone with opening angle Ψ, which is centered on the tangent to the orbit (Figure 2.3). Ψ can be expressed at the critical wavelength – λ_c (equation 2) – approximately by the so-called γ-ratio:

$$\Psi \approx \gamma^{-1} = (1957E)^{-1} \tag{1}$$

where E is the energy of the electrons (GeV). The critical wavelength, λ_c (nm), is defined at the wavelength where half of the total power is emitted according to:

$$\lambda_c = 0.559(R/E^3) \tag{2}$$

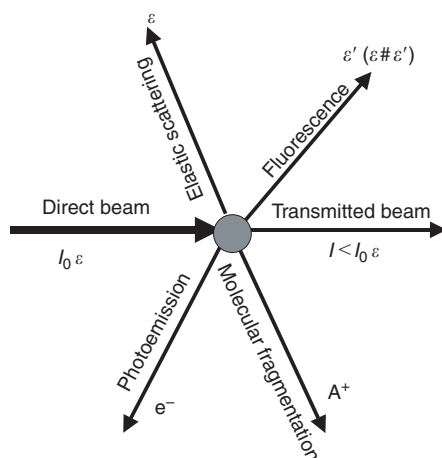[1] Defined as: photons/s/mrad^2/mm^2/0.1% bandwidth.

Figure 2.1 Schematic description of interaction modes of an X-ray photon beam with matter (I_0, incident beam intensity; I, transmitted beam intensity; ε, energy; A^+, ionized molecular fragment; e^- electron).
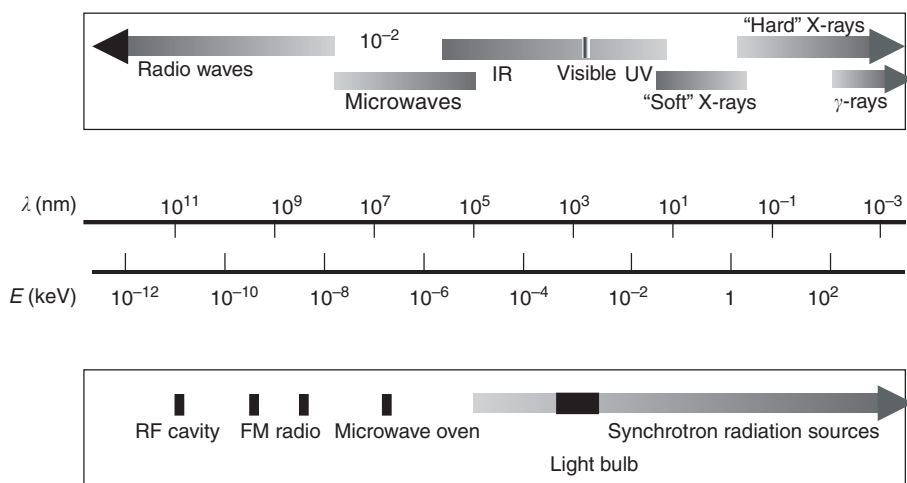

Figure 2.2 Spectral range of SR as compared to other radiation sources. The spectral range of soft X-rays is considered to start at wavelengths larger than about 0.25 nm, which corresponds roughly to the spectral cutoff of a Be-window separating the machine vacuum from the beamline. Conversion: $\lambda(\text{nm}) \approx 1.24/E(\text{keV})$.

where R (m) is the radius of curvature of the electrons in the bending magnet. The variation of λ_c with energy implies that several GeV of electron energy are required in order to obtain a sufficiently powerful beam in the hard X-ray regime.

Synchrotron radiation is usually generated in an electron storage ring, which is shown schematically in Figure 2.4. The polygon shape is characteristic for third generation SR sources (see Figure 2.8). The electron beam is guided from one straight section into the next by dipole magnets. Further, correcting magnets (quadrupole/hexapole magnets), are
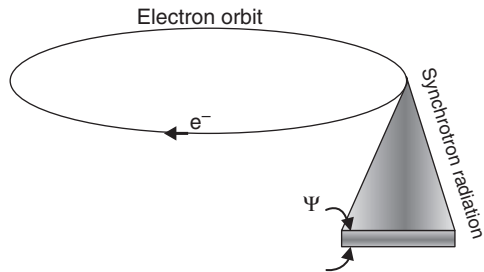
Figure 2.3 Schematic design of SR emission by a beam of electrons circulating at relativistic energies on a circular orbit. Ψ is the natural opening angle.
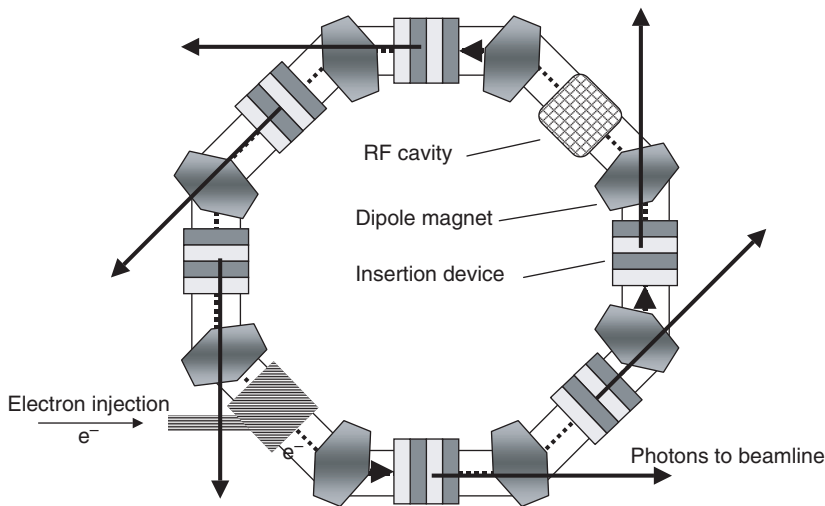

Figure 2.4 Schematic design of a SR storage ring. The main radiation sources are insertion devices, which are installed in the straight sections. Dipole magnets guide the electron beam from one straight section into the next.

not shown. The straight sections contain so-called *insertion devices* as principal radiation sources. Energy lost by the electron beam through SR is compensated by radio frequency (RF) cavities.

Insertion devices consist of a periodic array of magnets, which force the electrons to follow an (approximately) sinusoidal path in the orbital plane of the storage ring (Figure 2.5). They can be characterized by the so-called deflection (or magnetic field) parameter) K:

$$K = \delta\gamma = 93.4 B_0 \lambda_0 \tag{3}$$

where B_0 is the peak magnetic field (Tesla), λ_0 the spatial period of the magnet (m) and δ the maximum deflection angle of the electron trajectory (Figure 2.5). Depending on the strength
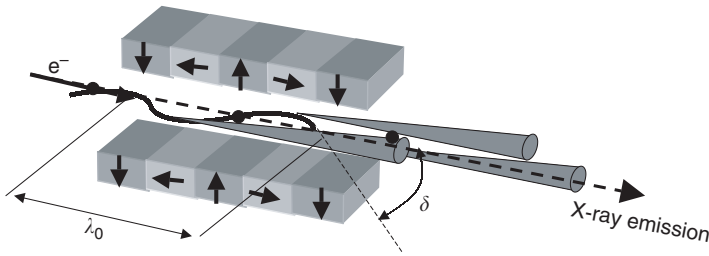
Figure 2.5 Periodic magnetic structure (period: λ_0) of an insertion device. Each arrow depicts the orientation of the magnetic field. The electron bunches follow a sinusoidal trace with a maximum deflection angle δ. Photon emission parallel to the electron path is indicated schematically at the inflection points. The opening angle of the emission corresponds to γ^{-1}.
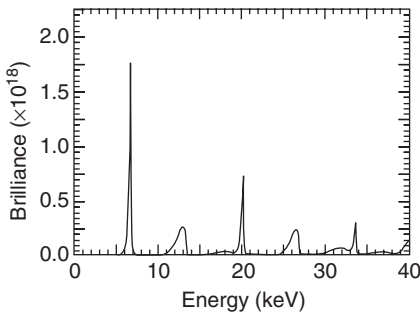

Figure 2.6 An undulator spectrum corresponds to a series of harmonics (example: undulator A at *Advanced Photon Source*). Brilliance: photons/s/mm^2/mrad^2/0.1% bandwidth.

of the magnetic field, and therefore, on the curvature of the sinusoidal track one can distinguish two operation regimes of insertion devices which are called *wigglers* or *undulators*:

Wiggler: High magnetic field with $\delta > \gamma^{-1}$. Only the points at the peak of the curve contribute to an emission of radiation into the observation direction. The distant observer will therefore "see" a multiplication of dipole sources.

Undulator: Weaker magnetic field with $\delta < \gamma^{-1}$. For this case, all points on the curve are emission points. This results in an interference phenomenon, which implies an emitted spectrum composed out of a series of harmonics (Figure 2.6).

Synchrotron radiation will also be observed from dipole magnets (not shown). For a dipole magnet or wiggler, the half-opening angle of the radiation in the vertical direction is γ^{-1} (equation 1) which corresponds to 85 μrad for a 6 GeV source such as the ESRF. In the horizontal plane, the photon emission has a spread of several milliradians. In contrast, the emission angle of an undulator is several tenth of microradians in both planes for the ESRF. Figure 2.7 shows the image of an undulator beam on a fluorescent screen at a distance of 31 m from the source [4]. The small emission angle results in an about 1 mm^2 spot size.
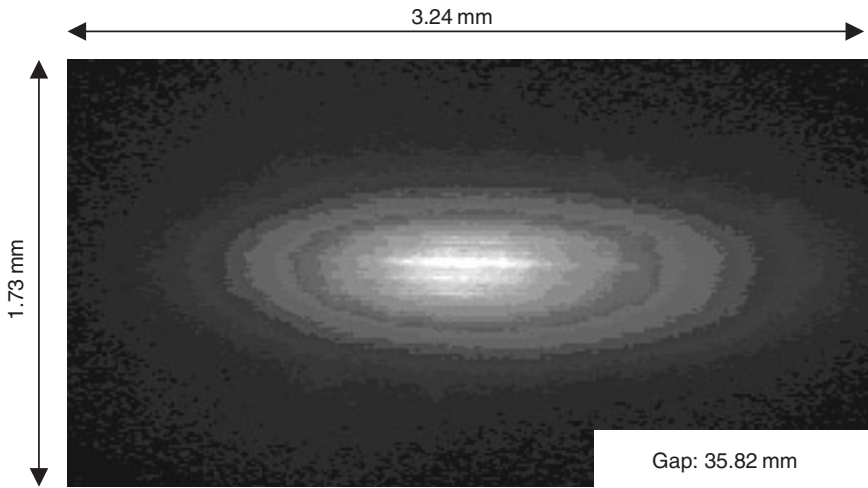
Figure 2.7 Image of an undulator photon beam on a fluorescence screen at 30.5 m from the undulator source point [4] (fifth harmonics; $\lambda_0 = 46$ mm; 35.82 mm gap between magnetic poles). (See Colour Plate III.)
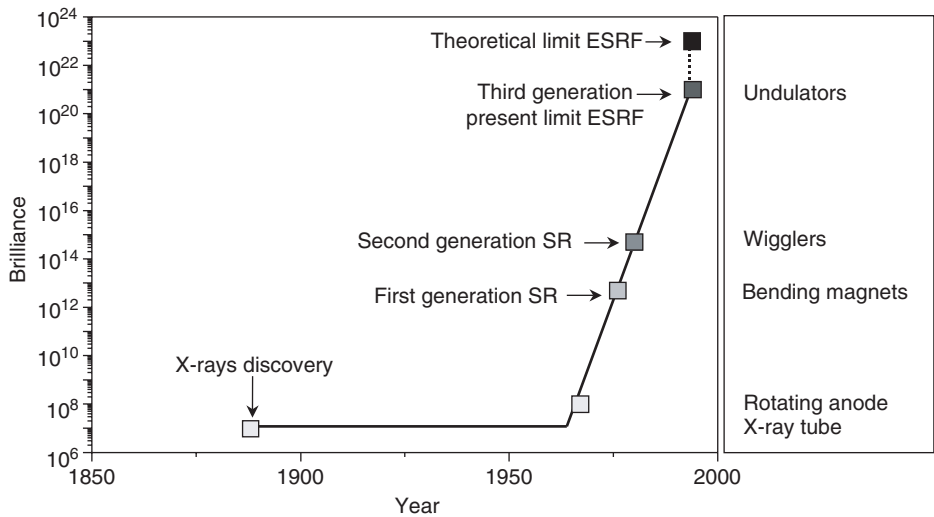

Figure 2.8 Increase of brilliance of X-ray sources since the discovery of X-rays. The principal radiation sources, which define the brilliance of the source, are indicated.

Figure 2.8 shows the nearly linear increase of brilliance of SR sources with time. Thus, the radiation from a dipole magnet at LURE is already a factor 10^4 times more brilliant than a rotating anode generator. Wigglers and, in particular, undulators have allowed further increases in the brilliance by a factor of 10^6, and the development is not finished as free electron laser sources are under development which are predicted to be up to a factor 10^6 times more brilliant and completely coherent [5].

2.3 Optics and instrumentation [6, 7]

Most SR experiments are performed with monochromatic, narrow bandwidth radiation. Wavelength (λ) and bandwidth ($\Delta\lambda = \lambda_{max} - \lambda_{min}$) selection relies on a monochromator, which is usually made out of one or more perfect crystals of silicon or germanium [8]. Bragg's law determines the wavelength at the exit of the monochromator:

$$n\lambda = 2d \sin\theta \tag{4}$$

where n is the order of a reflection, d the distance between the lattice planes and θ is the Bragg angle. Thus, the reflection condition is fulfilled at $\lambda = 0.15$ nm for the (111) lattice plane of a Si-monochromator with $d = 0.313$ nm at $\theta = 13.9°$. The bandwidth is $\Delta\lambda \approx 10^{-4}$ at this wavelength. One should note, however, that some experiments require polychromatic radiation with a large bandwidth. Both monochromatic and polychromatic radiations are for example used in diffraction experiments (Figure 2.9). For experiments with monochromatic radiation, the detector has to cover a large 2θ-range. This implies either a zero-dimensional (0D) detector, which is rotated through the 2θ-range or a 1D, or 2D detector, which covers the 2θ range for a single setting. For polychromatic radiation, all harmonics allowed by Bragg's law will be superimposed. A separation is, however, possible by a 0D detector with energy resolution. Polychromatic radiation is for example of interest for experiments with restricted access to the sample, such as high-pressure or chemical reaction cells. This compensates the generally lower order resolution and the limited 0D detector counting rate.

In order to increase the flux at the sample position one can focus the beam by a curved monochromator [8]. Another possibility is to use a mirror, which is curved in 1D (e.g. cylindrical shape) or 2D (e.g. toroid).

Mirrors reflect X-rays by total reflection below a critical angle Θ_c:

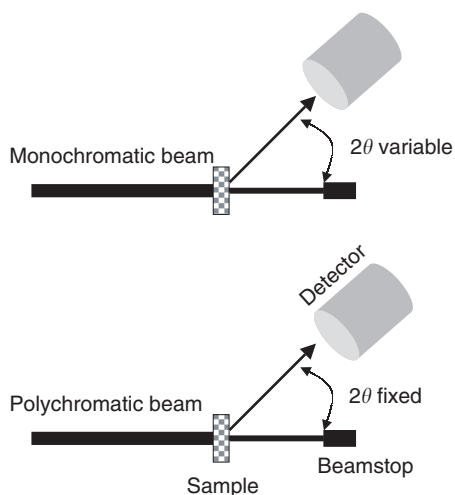$$\Theta_c = (20/E)\sqrt{\rho}\,(\text{mrad}) \tag{5}$$

Figure 2.9 Schematic display of diffraction setup for monochromatic and polychromatic radiation. The Bragg angle θ is fixed for the latter case.
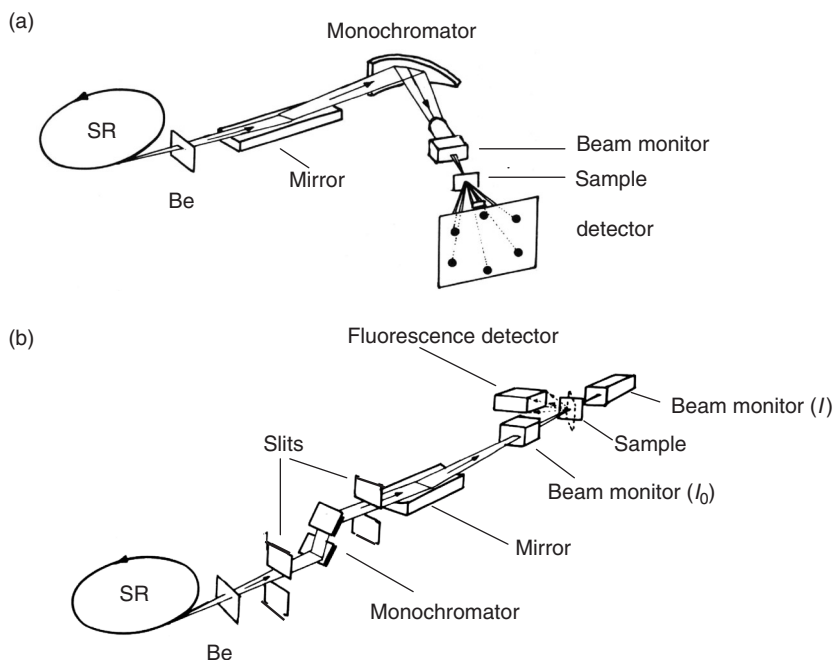
Figure 2.10 (a) SR beamline optimized for flux density. Be corresponds to the beryllium window separating the machine vacuum from the beamline. (b) SR beamline optimized for beam stability over an extended spectral range as required for the recording of EXAFS spectra with monochromatic radiation. (Adapted from [7].)

where E is the radiation energy (keV) and ρ the surface density (g/cm^3). For a glass surface, Θ_c corresponds to about 2.5 mrad at 0.1 nm wavelength [9]. An advantage of a mirror as compared to a focusing monochromator is the greater flexibility with respect to different wavelength and bandwidth.

A large number of combinations of mirrors and monochromators exist for specific applications. Only two typical examples will be mentioned. Figure 2.10(a) shows a double-focusing beamline, which has been optimized for flux density at the sample position [7, 10]. It uses a cylindrical mirror for focusing in the vertical plane and a cylindrically curved monochromator for focusing in the horizontal plane. Such optics are typically installed at a dipole magnet in order to capture a large angular range of the photon beam in the horizontal plane. The scattering pattern is recorded by a 2D detector. Depending on the application this could be a gas-filled detector, an image plate, or a charge-coupled device (CCD). An ionization chamber is used to monitor the flux on the sample continuously. Such a beamline can be used, for example, for protein crystallography [11] or real-time diffraction experiments during polymer crystallization [12].

Figure 2.10(b) shows a beamline optimized for absorption spectroscopy (EXAFS: extended X-ray fine structure analysis) [7]. The aim is to determine X-ray absorption for a more or less extended spectral range. In order to change the wavelength, while keeping the beam position at the sample constant, a double monochromator is used. A toroidal mirror is used for focusing in the horizontal and vertical planes. The sample absorption is determined by

two ionization chambers, one upstream and another downstream from the sample. A third ionization chamber allows measurement of the fluorescence signal.

2.4   Applications of synchrotron radiation in materials research

A number of applications making use of the brilliance and extended spectral range of SR will be mentioned below. Special emphasis has been put on imaging and real-time experiments using the hard X-ray spectrum, where the high brilliance of an SR source is of particular importance. A more complete list of SR applications in materials research can be found in the Appendix.

2.4.1   *Computed microtomography (μ-CT) [13, 14]*

Computed tomography (CT) with monochromatic radiation permits distinguishing of the composition and density of an object by the attenuation of an X-ray beam. The "image" of the object can be spatially reconstructed from measurements performed at different rotation angles. This method is used in medical applications but also to verify the integrity of structural materials.

Microtomography (μ-CT) extends tomography to high spatial resolution. This becomes possible by a high brilliance source, which allows use of an intense microbeam. Spatial resolution at SR sources using a parallel, monochromatic beam is limited by the detector resolution to about $1\,\mu$m. One can, in addition visualize selectively certain elements by making use of their absorption edges. Figure 2.11 shows schematically a μ-CT setup, based on a parallel beam and a 2D detector [13].

An interesting use of μ-CT for the petrol industry is visualization of the pore structure of materials. This gives important information for the modelling of macroscopic properties, such as the transport of liquids. Figure 2.12 shows the reconstructed image of a Fontainebleau stone [15]. A $5 \times 5\,\mu$m^2 beam was used. The resolution is about $10\,\mu$m. The fluid permeability calculated from these results agrees quite well with experimental data.
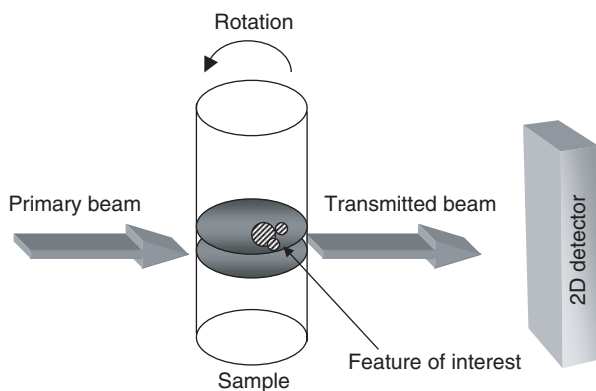

Figure 2.11 Schematic design of a microtomography setup. The beam transmission is measured for different rotation angles and at different heights. Image reconstruction allows localizing the feature of interest. (Adapted from [13].)
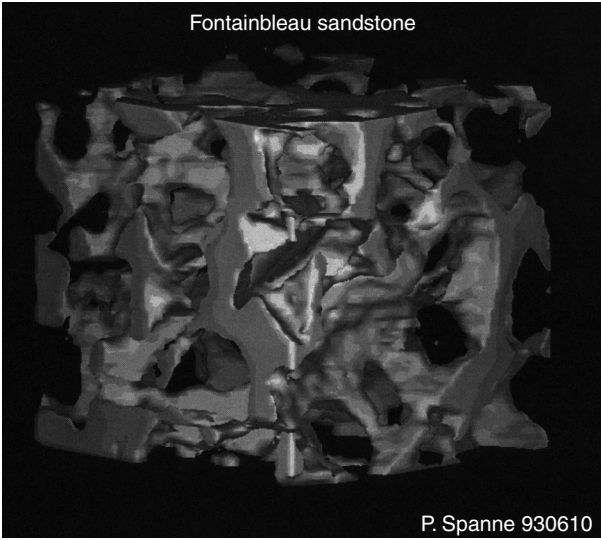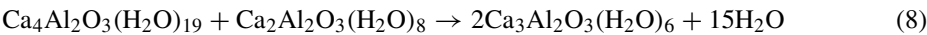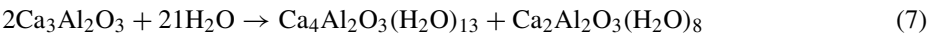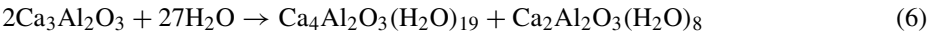
Figure 2.12 Example of image reconstruction based on a microtomography experiment: pore structure of a Fontainebleau stone [15]. (See Colour Plate VIII.)

2.4.2   *Time-resolved diffraction [16]*

Time-resolved (or real-time) diffraction provides a method of visualizing a phase transformation or chemical reaction and, thus, allows development of a microscopic model for the structural evolution being studied. The temporal length of the photon pulses, which are down to 60 ps for the ESRF storage ring, determines the ultimate temporal resolution. This resolution is, for example, required to study fast structural processes in proteins, which are initiated by a laser flash [17].

The formation of Portland cement, a technologically important material, takes place on a much slower time-scale. The overall reaction continues for several hours, but a fast onset reaction takes place within several seconds. This fast reaction could be followed in real time with a setup shown schematically in Figure 2.13 [18]. The optical system provides a polychromatic radiation band. Slits in front of the sample and between sample and detector allow defining the irradiated volume.

The hydration of cement is influenced in particular by the most reactive component $Ca_3Al_2O_3$. Chemical techniques allow isolating a number of hydrated phases of cement. Time-resolved diffraction allows in addition determining the succession of crystalline phases. Figure 2.14 shows a sequence of energy-dependent diffraction patterns recorded during the rapid hydration phase. Setting aside the phases $Ca_3Al_2O_3$ and $Ca_3Al_2O_3(H_2O)_6$, one observed only one intermediate phase which can be identified as $Ca_2Al_2O_3(H_2O)_8$. This phase acts obviously as nucleation phase for the end product $Ca_3Al_2O_3(H_2O)_6$. The reaction involving crystallographic phases can thus be formulated in the following way:

$$2Ca_3Al_2O_3 + 27H_2O \rightarrow Ca_4Al_2O_3(H_2O)_{19} + Ca_2Al_2O_3(H_2O)_8 \tag{6}$$

$$2Ca_3Al_2O_3 + 21H_2O \rightarrow Ca_4Al_2O_3(H_2O)_{13} + Ca_2Al_2O_3(H_2O)_8 \tag{7}$$

$$Ca_4Al_2O_3(H_2O)_{19} + Ca_2Al_2O_3(H_2O)_8 \rightarrow 2Ca_3Al_2O_3(H_2O)_6 + 15H_2O \tag{8}$$
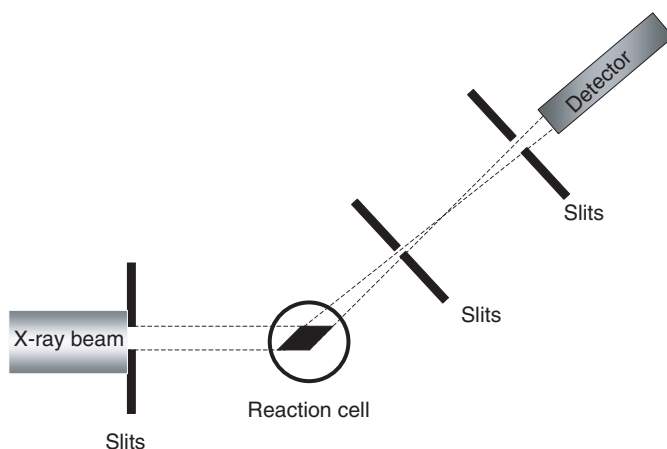
Figure 2.13 Schematic design of an experimental setup to follow the hydration of cement in real-time. The lozenge type "observation" volume in the cell is defined by the system of slits. (Adapted from [18].)
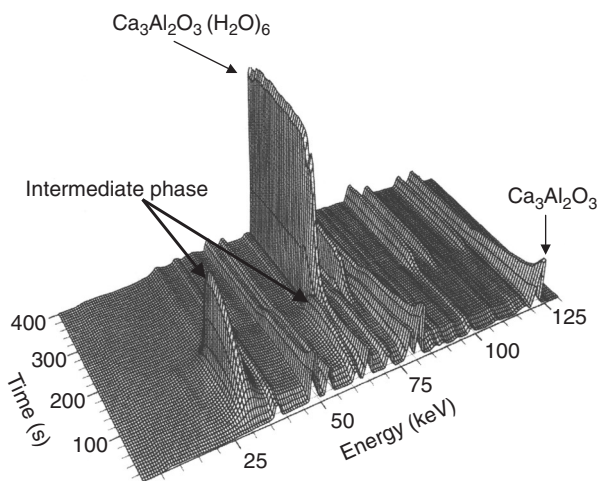

Figure 2.14 Temporal evolution of crystalline structures during the hydration of $Ca_3Al_2O_3$ as recorded by energy dispersive diffraction. (Adapted from [18].)

2.4.3   X-ray microdiffraction (μ-XRD)

X-ray microdiffraction allows us to study the local structure and orientation of materials or to investigate microcrystals [19]. Scanning μ-XRD is used to map an extended sample and to record at every position a diffraction pattern with a fast 2D-detector. This allows us to "image" the variation of the local structure and texture across the sample. Current technology employs beam sizes down to about 1 μm and submicron beam optics is under development [19–21]. A typical scanning setup is shown in Figure 2.15. In contrast to electron scattering techniques, the sample is scanned through a stationary beam. In this case a monochromatic beam, which
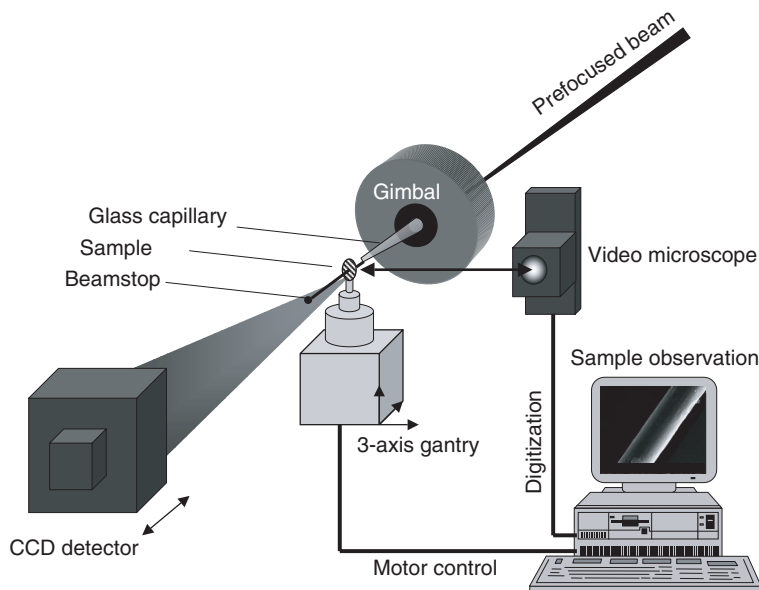
Figure 2.15 Schematic design of a scanning μ-XRD setup. The beam size can be defined by a glass capillary to about 1 μm at the sample position. The distance between the video microscope and beam position is calibrated which allows placing of the sample with micrometer accuracy in the beam. (Adapted from [19].)

has been focused to about 30 μm by a mirror, is further reduced to about 2 μm by a tapered glass capillary [19].

The scanning of a single fiber of the synthetic polymer ultrahigh molecular weight poly-ethylene (UHMW-PE) provides an example. A local area diffraction pattern of a UHMW-PE fiber is shown in Figure 2.16(a) [19]. The reflections correspond to the two crystalline phases of polyethylene: the orthorhombic phase and a metastable monoclinic phase. The monoclinic phase is formed by plastic deformation of the orthorhombic phase [22, 23]. The intensity ratio of the monoclinic phase (001) reflection and the orthorhombic phase (110) reflection – $I^{\mathrm{m}}_{001}/I^{\mathrm{o}}_{110}$ – is shown in Figure 2.16(b). Assuming cylindrical symmetry, the monoclinic phase appears to form a band extending along the fiber axis. This information could be obtained without sectioning the sample as required for electron diffraction techniques.

Scanning μ-XRD at high energies ($E > 50$ keV) with depth selection by conical slits has been developed for texture and strain mapping of bulk materials in volume with a spatial resolution of $5 \times 5 \times 50 \, \mu\mathrm{m}^3$ [24]. Spatial resolution of about 0.1 μm and smaller can be obtained in one direction by X-ray waveguide structures. This has been used to study buried strain fields in semiconductor devices [25].

2.4.4   *X-ray microfluorescence (μ-XRF)*

X-ray fluorescence (XRF) is based on X-ray photoionization of elements and the detec-tion of their characteristic fluorescent radiation. Excitation can be done both by white or monochromatic radiation. In contrast to electron probe microanalysis, XRF allows
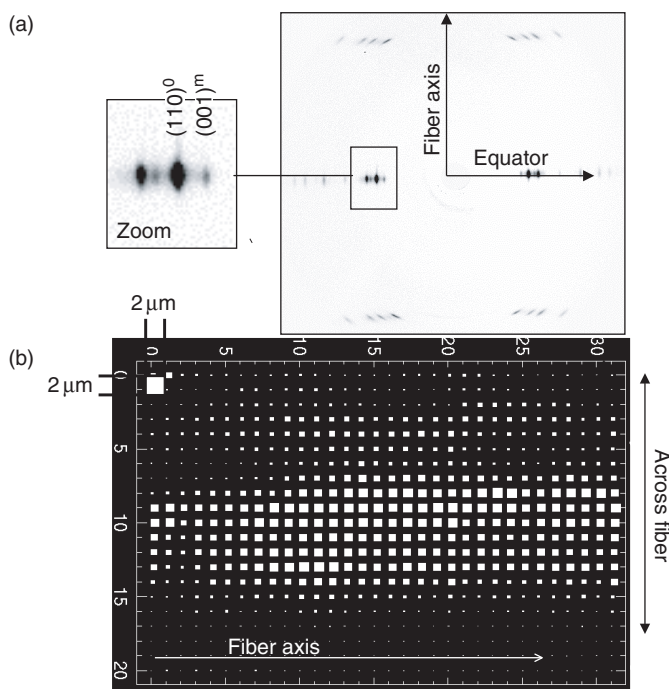
Figure 2.16 (a) Fiber diffraction pattern of a UHMW-PE fiber. The pattern shows reflections of the monoclinic and orthorhombic phases. (b) Distribution of the ratio monoclinic/orthorhombic phase calculated from the intensity ratio of a Bragg reflection of each phase across a single fiber on a mesh of $2 \times 2 \,\mu m^2$.

quantitative elemental bulk analysis down to the sub-ppm level [26, 27]. In exceptional cases, absolute detection limits in the range of $\leq 100 \, \mathrm{ag} (10^{-18} \, \mathrm{g})$ can be reached [28]. The same type of scanning system as used in scanning μ-XRD (Figure 2.15) in combination with an energy dispersive X-ray detector can be used for scanning μ-XRF [26, 29]. One obtains thus an "image" of the elemental distribution across the sample. Three-dimensional image reconstruction based on μ-XRF data obtained at different sample rotation angles has been demonstrated [26].

Figure 2.17 shows the result of a 2D scan of spruce wood cells through a $2 \times 2 \,\mu m^2$ monochromatic beam. X-ray microfluorescence images were obtained with traces of Mn and Fe in the cell walls at the 100 ppm level [30]. This information is of great interest for products derived from wood such as the production of pulp where the bleaching process by H_2O_2 can be influenced by the presence of transition metals. In a related experiment, the orientation of cellulose fibrils in wood cell walls has been determined by scanning μ-XRD [31]. Combined μ-XRF and μ-XRD experiments are, in principle, possible [32].

2.4.5 *Extended X-ray absorption fine structure (EXAFS) [7]*

X-ray absorption is dominated by the photoelectric effect up to about 0.03 nm. The absorption of a photon with a specific energy by an atom (Figure 2.18(a)) can liberate a
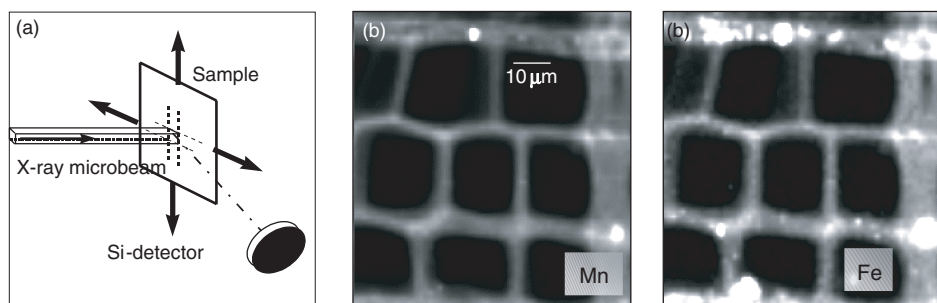
Figure 2.17 Imaging of wood cell walls for the Mn- and Fe-fluorescence on a mesh of $2 \times 2\,\mu m^2$ at $\lambda = 0.0984\,nm$. The cell walls of wood can be clearly distinguished. Bright spots correspond to larger particles containing Fe or Mn [30].
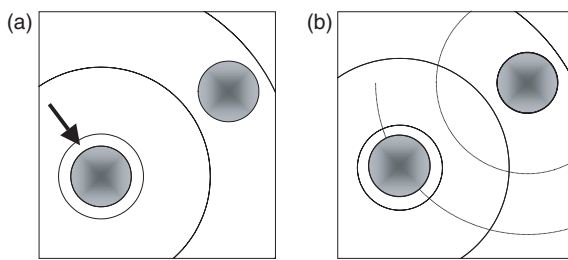

Figure 2.18 Principle of X-ray absorption spectroscopy: (a) after the absorption of a photon by the atom at the center, a photoelectric wave is created; (b) the reflection of this wave by the environment of the central atom is at the origin of the observed interference phenomenon.

photoelectron with a characteristic energy. The neighbouring atoms reflect the photoelectron wave (Figure 2.18(b)). The interference of the two waves creates an absorption spectrum, which allows extraction of the EXAFS function (Figure 2.19). The oscillations of this function extend up to $1000\,eV$ beyond the absorption edge (K, L, M, ...). In practice, one can transform the EXAFS function into real space by a Fourier transformation (Figure 2.19) [33]. This function is close to the pair correlation function of the central atom with its environment. A structural analysis allows us in principle to obtain information on the first coordination sphere of an atom (number of atoms, geometry and distances). The interest in such an analysis is due to the fact that one can analyze in principle for every atom its sphere of coordination.

Figure 2.20 shows the EXAFS-spectra at the L_3 edge of uranium in a uranium silicate glass [34]. The patterns were obtained at different incidence angles. For a large incidence angle the spectrum (a) reflects the bulk environment of uranium. Spectrum (b) was obtained for grazing incidence and reflects the local structure at the surface. The other spectra correspond to different degrees of corrosion and can be related to the formation of a gel at the surface. The increase in U–U correlation at the surface suggests the formation of clusters containing uranium atoms.
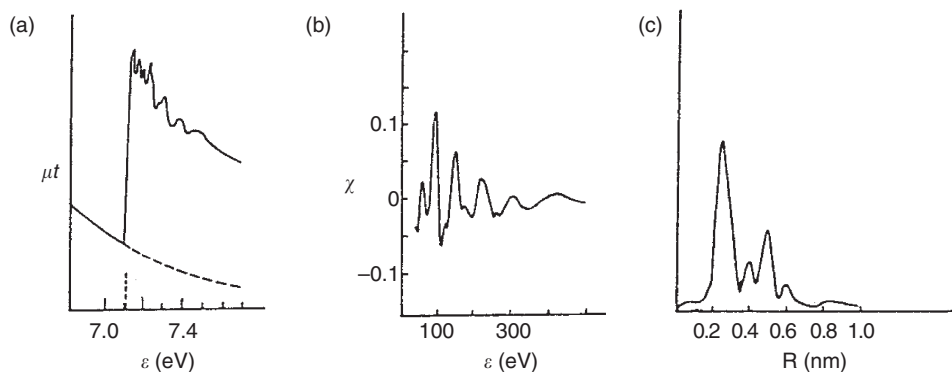
Figure 2.19 (a) Absorption spectrum at the K-edge of iron (μ, linear absorption coefficient; t, thickness of sample). (b) EXAFS function – $\chi(\varepsilon)$ – extracted from the total spectrum. (c) Fourier transformed EXAFS function. (Adapted from [33].)
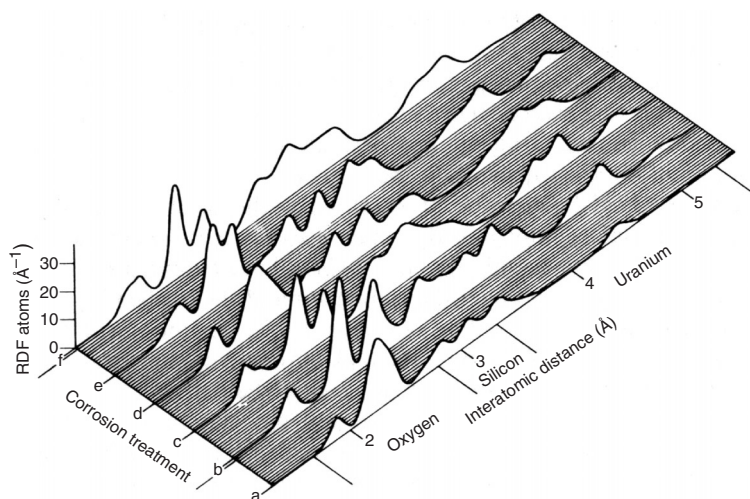
Figure 2.20 Fourier transformed EXAFS spectra of uranium silicate glasses: (a) bulk structure; (b) surface structure; (c–f) surface structures at different corrosion times [34].

Appendix

Synchrotron radiation applications in materials research

Diffraction [35, 36]

> Crystal structures of single crystals, powders and fibers
> Time-resolved and *in situ* diffraction
> Structures at high pressures
> Distinction of neighbouring elements by exploiting anomalous dispersion
> Microdiffraction with beam sizes extending into the submicron range

Structures of surfaces and interfaces by glancing incidence diffraction
Analysis of textures and strain distribution including experiments with microbeams [37]

Diffuse scattering [38–40]

Small-angle scattering
Defects in metals and alloys
Polymer crystallization
Structures of colloidal systems and emulsions

Extended X-ray absorption Fine structure (EXAFS) [33, 41]

Short-range correlation
Kinetics of phase formation
Local structure of catalysts

Topography [42, 43]

Defects in crystals
Analysis of dislocations and stress

Tomography [13, 14]

Three-dimensional reconstruction of materials based on absorption or phase contrast.

Microfluorescence [26, 44]

Quantitative analysis of elements
Elemental mapping with beam sizes extending into the submicrometer range

Lithography [45]

Production of artificial structures in three dimensions (LIGA process)
Microlithography applications in semiconductor industry

References

[1] Kunz C., Properties of synchrotron radiation, in *Synchrotron Radiation – Techniques and Applications*, C. Kunz (ed.), 1979, Springer Verlag: Berlin. pp. 1–24.

[2] Winick H., Properties of synchrotron radiation, in *Synchrotron Radiation Research*, H. Winick and S. Doniach (eds), 1980, Plenum Press: New York. pp. 11–26.

[3] Krinski S., Perlman M. L. and Watson R. E. (eds), Characteristics of synchrotron radiation and its sources, in *Handbook on Synchrotron Radiation*, E. E. Koch (ed.), Vol. 1b, 1983, North-Holland: Amsterdam, pp. 65–172.

[4] Webpage: http://www.esrf.fr/machine/support/ids/Public/ID6Movies/ID6movies.html

[5] Tatchyn R. *et al.*, X-ray optics design studies for the 1.5 to 15 A Linac coherent light source (LCLS) at the Stanford Linear Accelerator Center (SLAC), in *Coherent Electron-Beam X-Ray Sources: Techniques and Applications*, 1997, SPIE Vol. 3154.

[6] Freund A., X-ray optics for synchrotron radiation, in *Neutron and Synchrotron Radiation for Condensed Matter Studies*, J. Baruchel *et al.* (eds), 1993, Springer Verlag: Berlin. pp. 79–94.

[7] Greaves G. N. and Catlow C. R. A., Synchrotron radiation instrumentation, in *Applications of Synchrotron Radiation*, C. R. A. Catlow and G. N. Greaves (eds), 1990, Blackie: Glasgow. pp. 1–38.

[8] Matsushita, T. and Hashizume, H. O., X-ray Monochromators, in *Handbook of Synchrotron Radiation*, E. E. Koch (ed.), Vol. 1b, 1983, North-Holland: Amsterdam. pp. 261–314.

[9] Webpage: http://www-cxro.lbl.gov/optical_constants/mirror2.html

[10] Rosenbaum G. and Holmes K. C., Small-angle diffraction of X-rays and the study of biological structures, in *Synchrotron Radiation Research*, H. Winick and S. Doniach (eds), 1980, Plenum Press: New York. pp. 533–564.

[11] Glover I. D. and Helliwell J. R., Protein crystallography, in *Applications of Synchrotron Radiation*, C. R. A. Catlow and G. N. Greaves (eds), 1990, Blackie: Glasgow. pp. 241–267.

[12] Elsner G., Riekel C. and Zachmann, H. G., Synchrotron radiation in polymer science, in *Advances in Polymer Science*, H. H. Kausch and H. G. Zachmann (eds), 1985, Springer: Berlin.

[13] Hmelo A. B., *J. X-ray Sci. Technol.* **4**, 290–300 (1994).

[14] Flannery B. F. *et al.*, *Science* **237**, 1439–1444 (1987).

[15] Spanne P. *et al.*, *Phys. Rev. Lett.* **73**, 2001–2004 (1994).

[16] Pannetier J., Time resolved experiments, in *Neutron and Synchrotron Radiation for Condensed Matter Studies*, J. Baruchel *et al.* (eds), 1993, Springer: Berlin. pp. 425–436.

[17] Srajer V. *et al.*, *Science* **274**, 1726–1729 (1996).

[18] Jupe A. C. *et al.*, *Phys. Rev. B* **53**, 14697–14700 (1996).

[19] Riekel C., New avenues in X-ray microbeam experiments, *Rep. Prog. Phys.* **63**, 233–262 (2000).

[20] *X-ray Microbeam Technology and Applications*, 1995, San Diego, CA: SPIE Vol. 2516.

[21] *X-ray Microfocusing: Applications and Techniques*, 1998, San Diego, CA: SPIE Vol. 3449.

[22] Turner-Jones A., *Science* **62**, S53–S56 (1962).

[23] Seto T., Hara, T. and Tanaka, K., *Jpn. J. Appl. Phys.* **7**, 31 (1968).

[24] Lienert U. *et al.*, A high energy X-ray microscope for the local structural characterization of bulk materials, 40th Conference of AIAA on Structures, "Structural Dynamics of Bulk Materials," 1999, St Louis (USA), 2067–2075.

[25] Di Fonzo S. *et al.*, *Nature* **403**, 638–640 (2000).

[26] Janssens K. H. A., Adams, F. C. V. and Rindby, A. (eds), *Microscopic X-ray Fluorescence Analysis*, 2000, John Wiley & Sons: Chichester.

[27] Vis R. D., Synchrotron radiation trace element analysis, in *Applications of Synchrotron Radiation*, C. R. A. Catlow and G. N. Greaves (eds) 1990, Blackie: Glasgow. pp. 311–332.

[28] Vekemans B., *et al.*, *Book of Abstracts*, EDXRS-2000, Krakow, Poland, 2000, p. 106.

[29] Rindby A., X-ray Spectometry, **18**(3), 187–191 (1993).

[30] Berlund A. *et al.*, *Holzforschung* **53**, 474–480 (1999).

[31] Lichtenegger H. *et al.*, *J. Appl. Crystallogr.* **32**, 1127–1133 (1999).

[32] Rindby A., Engström P. and Janssens K., *J. Synchrotron Radiat.* **4**, 228–235 (1997).

[33] Gurman S. G., EXAFS and structural studies of glasses, in *Applications of Synchrotron Radiation*, C. R. A. Catlow and G. N. Greaves (eds), 1990, Blackie: Glasgow. pp. 140–170.

[34] Greaves G. N., *J. Am. Chem. Soc.* **111**, 4313 (1998).

[35] Catlow C. R. A., X-ray diffraction from powders and crystallites, in *Applications of Synchrotron Radiation*, C. R. A. Catlow and G. N. Greaves (eds), 1990, Blackie: Glasgow. pp. 1–38.

[36] Coppens P., *Synchrotron Radiation Crystallography*, 1992, Academic Press: London.

[37] Heidelbach F., Riekel, C. and Wenk, H. R., *J. Appl. Crystallogr.* **32**, 841–849 (1999).

[38] Lambert M., Diffuse scattering, in *Neutron and Synchrotron Radiation for Condensed Matter Studies*, J. Baruchel *et al.* (eds), 1993, Springer Verlag: Berlin. pp. 223–234.

[39] Williams C., Small angle scattering from solids and solutions, in *Neutron and Synchrotron Radiation for Condensed Matter Studies*, J. Baruchel *et al.* (eds), 1993, Springer Verlag: Berlin. pp. 235–245.

[40] Russell T. P., Small-angle scattering, in *Handbook of Synchrotron Radiation*, G. S. Brown and D. E. Moncton (eds), Vol. 3, 1991, North-Holland: Amsterdam. pp. 379–470.

[41] Stern E. A. and Heald S. M., Basic principles and applications of EXAFS, in *Handbook of Synchrotron Radiation*, E. E. Koch (ed.), Vol. 1b, 1983, North-Holland: Amsterdam. pp. 955–1014.

[42] Miltat J. and Dudley M., X-ray topography, in *Applications of Synchrotron Radiation*, C. R. A. Catlow and G. N. Greaves (eds.), 1990, Blackie: Glasgow. pp. 65–99.

[43] Baruchel J., Neutron and synchrotron radiation topography, in *Neutron and Synchrotron Radiation for Condensed Matter Studies*, J. Baruchel *et al.* (eds), 1993, Springer Verlag: Berlin. pp. 79–94.

[44] Baryshev V., Kulipanov G. and Skrinsky A., X-ray fluorescent elemental analysis, in *Handbook of Synchrotron Radiation*, G. S. Brown and D. E. Moncton (eds), Vol. 3, 1991, North-Holland: Amsterdam. pp. 639–688.

[45] Grobman W. D., Synchrotron radiation X-ray lithography, in *Handbook of Synchrotron Radiation*, E. E. Koch (ed.), Vol. 1b, 1983, North-Holland: Amsterdam. pp. 1131–1165.